PHYSICAL REVIEW A VOLUME 28, NUMBER 2 AUGUST 1983

Detailed observation and analysis of radiation from high-density laser-imploded targets

Allan Hauer
Los Alamos National Laboratory, University of California, Los Alamos, New Mexico 87545

K. G. Whitney, P. C. Kepple, and J. Davis
U.S. Naval Research Laboratory, Washington, D.C. 20375

(Received 22 November 1982)

High-energy CO_2-laser radiation has been used to implode gas-filled spherical targets to very high densities ($10^{23} < n_e < 10^{24}$ cm^{-3}) and temperatures (~ 800 eV). The imploded gas was composed primarily of DT with a small amount of argon seed. The detailed observation of radiation from the argon was a primary diagnostic of the imploded-plasma conditions. An extensive analysis of the emitted argon spectrum provides a rich source of information on plasma parameters. In most cases one could not assume local—thermodynamic-equilibrium conditions. A very detailed collisional-radiative model was constructed in order to analyze the spectrum. In view of the complexity of the calculations that had to be performed and the care needed in data acquisition and processing, the agreement between theory and experiment was very good.

I. INTRODUCTION

Laser-driven implosions have produced high-temperature compressed plasmas with densities comparable to or greater than ordinary solids (a few g/cm^3).[1-3] A whole new regime of very high-density, high-temperature plasma conditions has thus been opened for laboratory investigation.

The production of very high-density compressed plasmas is central to the inertial-confinement fusion concept. Analysis of the radiation from these dense plasmas is an important source of information on their conditions. This analysis may, however, involve relatively complicated modeling techniques. In this paper we describe techniques that have proved useful in the modeling of radiation from compressed plasmas with a density of a few gm/cm^3. The experiment analyzed here has been reported previously.[2]

In Fig. 1, we show a typical target used in high-compression laser-implosion experiments. The targets are imploded by irradiating them with high-intensity CO_2-laser light from the Los Alamos National Laboratory Helios laser facility. Laser energy on target ranged from 3—6 kJ and the half width of the pulse was 600—800 ps.

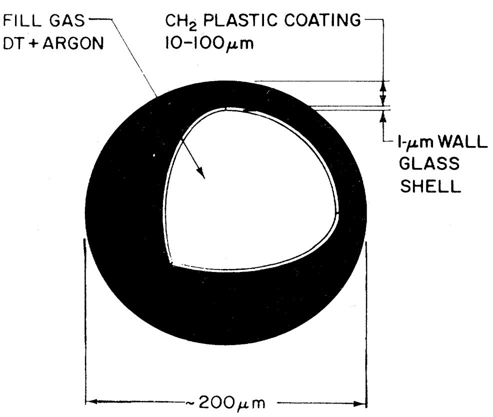

FIG. 1. Target used to produce high-density laser-driven implosions.

Within the target is a glass shell filled with a variety of gases; DT is used as the fuel for thermonuclear burn. Spectroscopic diagnosis of plasma temperature and density is accomplished by seeding the DT fuel with a small amount of higher Z material, such as neon or argon. Analysis of line emission from the higher Z material is one of the most direct diagnostics of compressed density.

The thick layer of plastic surrounding the glass shell reduces the preheat of the fuel due to suprathermal (~ 100 keV) electrons and allows an ablative implosion of the shell. In earlier work of this type[4] only the thin glass shell was present. Long-mean-free-path electrons tended to uniformly heat and thus explode this shell. In the present work a slower less explosive implosion[2] has produced considerably higher densities of the order of 20 times the liquid density.

In Fig. 2, we show the general features of argon emission from highly compressed plasmas. The top trace was taken with an exploding pusher target irradiated by about 3.5-kJ laser energy on target and represented a compressed electron density of about 9×10^{22} cm^{-3}. The middle trace was obtained from a target with a coating of 25-μm $(CH_2)_x$ (and 4.5-kJ laser energy on target). The compressed electron density here is about 4×10^{23} cm^{-3}. The final trace was produced by a target with 50-μm $(CH_2)_x$ coating and about 5.8 kJ of laser energy. The compressed electron density is about 7×10^{23} cm^{-3}. In the experiment represented by the top trace of Fig. 2 the laser heats the glass shell directly; lines due to calcium and potassium, which are impurities in the glass, are excited. When a layer of about 25 μm of plastic is added these lines are suppressed.

The densities in these experiments[2] were measured primarily by fitting time integrated x-ray spectral profiles to theoretical calculations. The theoretical calculations were made for specific densities and did not attempt to take

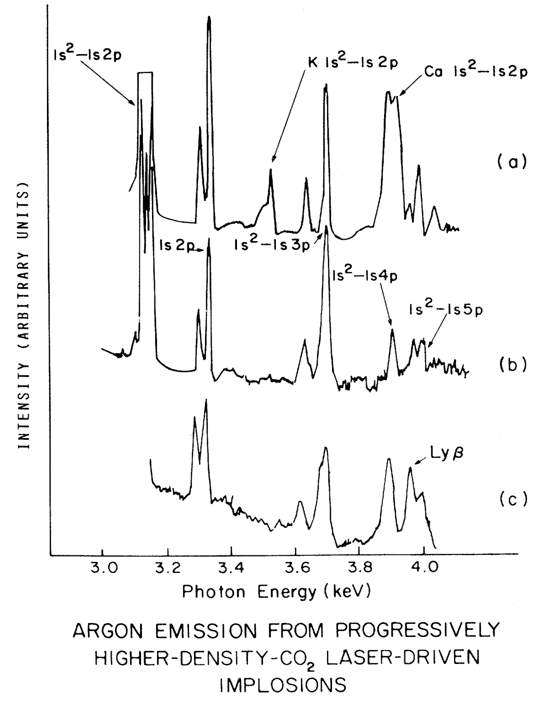

FIG. 2. Argon emission from progressively higher-density CO_2-laser—driven implosions. (a) Glass microballoon without plastic coating, (b) microballoon coated with 25-μm $(CH_2)_x$, and (c) microballoon coated with 50-μm $(CH_2)_x$. Unmarked lines are from argon.

into account the complete variation of density during the implosion. Densities were also estimated from x-ray pinhole photographs. A more complete description of these experiments is given in Ref. 2.

When attempting to make very detailed comparisons between theory and experiment for laser plasmas, the question of non-LTE (local—thermodynamic-equilibrium) behavior inevitably arises. It has been shown that even in the exploding pusher case (where neon was often used as the fill gas) non-LTE analysis must be performed if experimental data is to be properly analyzed and very accurate information is desired.[5] In the case of higher-density work utilizing argon emission this is shown below to be even more important.

Simple considerations give an indication of the importance of non-LTE analysis. For a level to be in collision-dominated (CD) equilibrium with higher levels, ignoring pressure ionization effects, we use the following criterion taken from Griem[6]:

$$N_e > 7\times 10^{18}\frac{Z^6}{(n)^{17/2}}\left[\frac{kTe}{Z^2E_H}\right]^{1/2}\ \text{cm}^{-3}\ , \tag{1}$$

where $Z-1$ is equal to the charge of the hydrogenic ion which is equal to 17, n is the principal quantum number, E_H is the ionization energy of hydrogen, and T_e is the electron temperature. For example, for $n=2$, $N_e > 4\times 10^{24}$, while for $n=3$, $N_e > 1.1\times 10^{23}$. The state $n=2$ is not in local thermodynamic equilibrium (LTE) with higher levels in the present experiments, while $n=3$ is usually close. The very large optical depth of the helium and hydrogenlike resonance lines does, however, bring $n=2$ much closer to LTE than it would otherwise be (through absorption out of the ground state). It is, thus, clear that in order to deal with questions such as the detailed transport of optically thick lines (e.g., Lyman α and $1s^2$-$1s2p$) a detailed non-LTE radiation model must be utilized.

II. EXPERIMENT AND ANALYSIS

The targets used in these implosion studies were generally of the construction described above. The diameter of the fuel region was about 200—250 μm. The plastic coating was between 15 and 50 μm.

The argon seed gas used for diagnostic emission in these experiments was initially at a few tenths of an atmosphere. The DT gas was at a pressure of approximately 30 atm. The partial pressure of the argon fill was controlled in order to give reasonably strong line emission while keeping the optical depths of important lines to a minimum. In Table I, we show approximate values for the optical depth of various lines (based on LTE calculations for a typical partial pressure of argon of 0.2 atm).

The primary experimental diagnostic used for determining core density was argon line spectra (2—4-keV range) measured with two crystal spectrographs. Pentaerythritol (PET) crystals employing the (002) reflection ($2d=8.74$ Å) were used. One of the devices used a slit for spatial resolution. Measurements of the size of the compressed core were used as an auxiliary indication of imploded density.[7] The core emission region was usually of the order of 20 μm in diameter.

The spectra were recorded on Kodak 2491 fine grain blue sensitive film. The fundamental signal-to-noise ratio is governed by the line-to-continuum (plus background) level. The background (in addition to the normal fog level of the film) is due primarily to hard x rays produced by the scattering of the suprathermal electrons.

There are two major contributions to the instrument profile: (a) source broadening (due to the finite size of the emitting source) and (b) the crystal diffraction curve. To obtain an estimate of source broadening we differentiate Bragg's law:

$$\frac{\Delta E}{E}=\frac{\Delta\lambda}{\lambda}=\cot\theta\,\Delta\theta,\quad \Delta\theta\approx\Delta x/L\ , \tag{2}$$

where Δx is the source dimension and L is the distance from source to film. The orthogonal spatial resolution (provided by the slit) allows rather accurate determination of the source size and thus the spatial broadening. In these experiments the source size (the radiating compressed core) was such that $\Delta E \sim 3.0$ eV. This is of

TABLE I. Optical depths of various argon lines for typical compressed electron densities.

Line	τ_0 (cm^{-1})
Lyα	13
Lyβ	0.25
$1s^2$-$1s2p$	150
$1s^2$-$1s3p$	0.5

the order of 10% of the broadest lines. The instrumental profile, including the actual source size relevant to particular shots, is carefully accounted for in the theoretical calculations.

In the present experiments the contribution from crystal broadening to the instrumental profile was small compared to the source broadening. The crystal PET (Ref. 8) has been shown (in relatively new samples) to have a rocking curve width corresponding to ΔE (in the present experiments) of about 0.2 eV. Although the particular crystals used in this experiment were not measured directly they were new enough that large departures from the above quoted figures would not be expected.

All of the spectral data described here is time integrated. Broadband time resolved measurements indicate that most of the emission in the spectral region of the argon lines tends to occur in a time interval of about 100 ps near peak compression (stagnation). This agrees with calculations described below.

In the remainder of this section we describe the procedures used in analyzing experimental spectra and processing of the data for comparison with theory. The first step in this analysis of the data is to make rough estimates of the average compressed temperatures and densities. Electron temperatures are measured by using both line ratios and continuum slopes. The continuum slope method is the most straightforward. It is sometimes compromised by hard x-ray background (due the aforementioned fast electrons). When special precautions (described below) are taken in subtracting the background, temperature determinations using continuum slope estimates of ±50-eV accuracy are possible. Line ratio measurements are complicated by the very dense plasma conditions. The high density causes only a relatively small number of members of a series to be present while causing the low quantum number transitions to be optically thick ($\tau_0 \gtrsim 10$). This usually makes ratios between ionization stages the best choice. This, of course, introduces a dependence on electron density and the self-consistency of density and temperature measurements must be carefully checked.

Line profiles are used as the primary indicator of density. Plasma temperatures during emission are of importance in the analysis of line profiles. In the present density regime (where Doppler broadening is negligible) the profile dependence on temperature is relatively weak and rough determinations of temperature are adequate.[9–11] As mentioned above, one or two lines of both the hydrogen and heliumlike Lyman series are usually optically thin. The fitting of one of these lines to a theoretically calculated profile is taken as a first indicator of the density. The density variation during compression (and thus during the period of line emission) causes the line fit to yield a temporally averaged value for density. In addition, temperature variations will cause various lines to be emitted at slightly different times. The fitting process also averages over spatial gradients within the compressed core. The complete theoretical modeling (described in Sec. III) takes into account both spatial and temporal influences on line emission.

In attempting to fit experimental data to theoretically calculated spectra, the following steps represent a typical procedure:

(a) The film is carefully scanned and digitized. The step size is usually taken to be that corresponding to a small fraction of the spectrograph resolution (using the known linear dispersion in $\Delta\lambda$/cm). The spectrograph is arranged so that the outline of the periphery of the crystal (produced by the radiation diffracted by the crystal) is visible on the film. Overall background radiation not diffracted by the crystal is thus easy to identify. A scan is then made of the background exposure adjacent to the spectrum. Once the film data has been recorded on tape a series of computer programs are used to reduce and analyze the data.

(b) The film data is first absolutely calibrated using data obtained from continuous-wave (cw) calibration tests.[12] The calibration tests have been performed with realistically narrow line exposures similar to spectral line profiles. In general, there does not seem to be any distortion of line profiles from photographic adjacency effects (variation in film calibration within small spatial scale exposures). Although the wavelength of the hard x-ray background is not known accurately, the film response does not vary much in this region and it is adequate to use an averge response. Background is then subtracted from the data.

The continuum level is manually estimated and subtracted from the main profile. Ideally, the continuum should be included as another parameter in the fitting procedure. The present procedure was felt to be adequate for the primary purpose of determining compressed density.

(c) The wavelength and dispersion are calibrated using known lines (and other features such as absorption edges). The position of the crystal with respect to the film is accurately known so that an exact fit can be obtained for a flat crystal. When curved cyrstals are employed the dispersion is determined by a least-squares fit to a polynomial. This procedure is done interactively on a computer terminal. The dispersion determined in this way is quite adequate for determining most profile characteristics. Subtle properties such as small line shifts, however, require greater care.

(d) The results of theoretical spectrum calculations convolved with the instrument function (these calculations are described in Sec. III below) made using various input assumptions are stored in computer memory. Estimates can now be conveniently made of the deviation between experimental and theoretical spectra. In fitting a particular line profile for a density measurement, we usually tabulate the normalized sum of squared deviations (referred to as the fit factor F).

This gives equal weight to deviations in all parts of the profile. It is clear that in many cases this criterion does not represent the best choice. For example, we are often aware of theoretical inadequacies near line center.[13,14] This factor seems reasonably adequate, however, in making estimates of the error in density measurements using profile fitting which is one of the most important applications of this type of spectral analysis. In Fig. 3, we show the result of noise being artifically superimposed on a theoretical profile (including the instrument function). A fit factor F is then calculated with this noisy profile as the input. This procedure establishes the role of data noise in the fitting (by using a noise amplitude compatible with a particular data set). In practice, F factors from actual fits

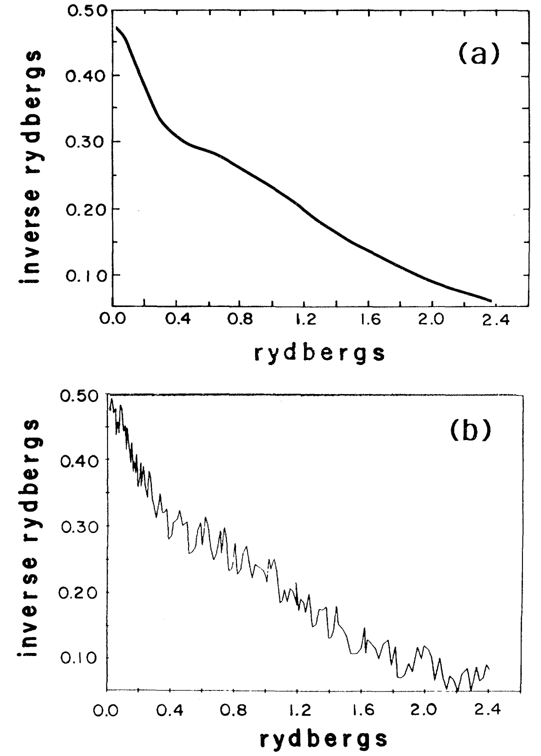

FIG. 3. (a) Theoretical argon Lyman γ profile and (b) profile with artificial noise introduced; using this as input to fitting procedure gives $F \sim 0.01$.

to experimental data rarely come within a factor of 2 of the lower bound established by this process.

III. THEORY

In order to calculate the radiation from these laser-driven implosions an extensive collisional-radiative (argon K-shell) model has been constructed. The time- and space-varying nature of the emitting region is included although the final comparison is with a time-integrated spectrum. By calculating a large number of spectral features (line intensities, profiles, etc.) a substantial confirmation of plasma conditions can be obtained.

The collisional-radiative model incorporates overall plasma conditions that are predicted by a one-dimensional version of the Lagrangian hydrodynamic code LASNEX.[15] Experimental measurements provided a substantial number of constraints on the choice of input conditions to these calculations. These measurements included (a) thermonuclear yield measurements, (b) ion temperature obtained from neutron broadening, (c) implosion times from time resolved neutron signals, (d) hot-electron temperature measurements, and (e) absorbed energy measurements. The calculational procedure is thus composed of two steps. LASNEX calculation of the overall plasma conditions (using experimental measurements in the choice of LASNEX initial conditions) constitutes the first step. In the second step, detailed radiation characteristics are calculated with the collisional-radiative (CR) model (using LASNEX-calculated input conditions).

The CR model is, at present, used in a post process mode where temperature and density output information from LASNEX (as a function of space and time) is processed separately and results are not fed back into the hydrodynamic code (the argon was a small percentage of the mass of the total fill gas).

The effects of departures from LTE on the overall energetics of the target are handled by using an average ion model.[16] This calculation is done in real time and the results are fed back into the hydrodynamic calculation.

The LASNEX hydrodynamic calculation and the CR calculation are both performed in 1D spherical geometry. A 1D Lagrangian mesh is set up which consists of spherical shells of radius R. Time histories of the central radii of the spherical shells, $R(i,t)$, the total electron densities $N_e(i,t)$, the electron and ion temperatures $T_e(i,t)$ and $T_i(i,t)$, and the total average charge states $Z(i,t)$ (for each of the 11 cells describing the Ar-DT core region of the microballoon, $i=1,\ldots,11$) were obtained from LASNEX calculations that were set up to model specific experimental laser shots. These quantities were then used as the input conditions for the emission spectrum calculations.

In the experiment that will be analyzed in detail here (and the corresponding LASNEX calculation) the gas-fill region of the target contained 50 DT molecules per 1 argon atom and about 6.3 nanograms of argon. Plots of $T_e(i,t)$, $N_{\mathrm{Ar}}(i,t)$, and $R(i,t)$ for a typical laser-driven implosion are shown in Figs. 4—6, respectively, over the time interval of specific interest (encompassing peak compression) to the emission of argon K-shell radiation in the 3- to 4.2-keV spectral interval. Each of the curves in these figures is labeled with its unique symbol so that for each temperature, argon densities and locations of each cell can be identified.

The K-shell emission calculation (corresponding to Figs. 4—6) was begun with the argon core at temperatures between 220—320 eV, densities below 1.5×10^{20} argon ions/cm^3, and with the core region already compressed to a radius of $R_0=65$ μm. It proceeded through the point of

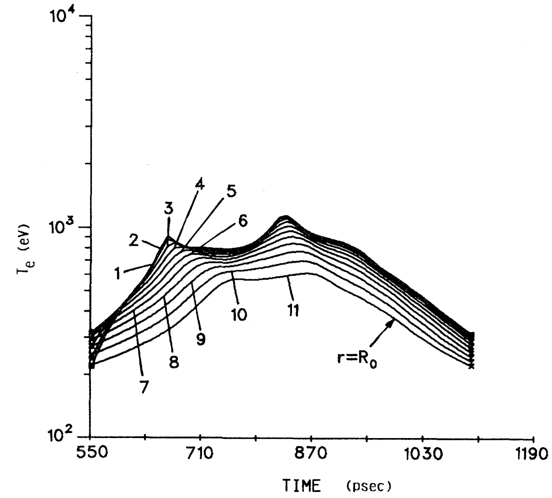

FIG. 4. Electron temperatures as a function of time for a typical high-density laser-driven implosion.

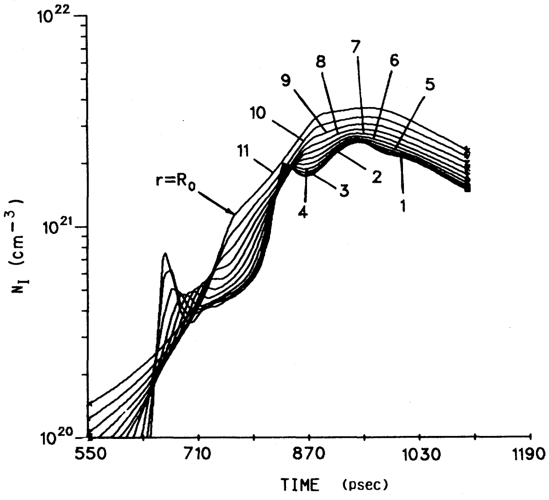

FIG. 5. Argon ion density as a function of time for the same implosion as Fig. 4.

peak compression, $R_0 = 19.6$ at 950 ps, where the argon density at $r = 0$ [the innermost cell whose cell "half center" is at $R(1,t) \sim 2$ μm] reached a peak value of 3.6×10^{21} cm^{-3}. A temperature peak at $r = 0$ of 1.3 keV was reached earlier in time at 832 ps. Note that the argon in contact with the glass wall remained the coolest region throughout the portion of the implosion shown in Fig. 4. The ion density, on the other hand, underwent several gradient reversals in this time interval due to the passage of shock and rarefaction waves.

In order to model the radiation produced by these complicated conditions, several important ingredients were contained in the radiation coupling and transport calculations. They included the calculation of high-density[9,10] Stark line profiles, the incorporation of oscillator strength sum rules, and of overlapping line and continuum emission and absorption processes.[5] These profile calculations included some of the first done for higher Z heliumlike emission (performed specially for the present study).[14,17,18] Accurate profiles are an important part of the spectrum calculations, since experimental line emission features are emphasized in this paper. In this study only relative comparisons between line features are made. Continuum emissions from the glass and plastic are not calculated.

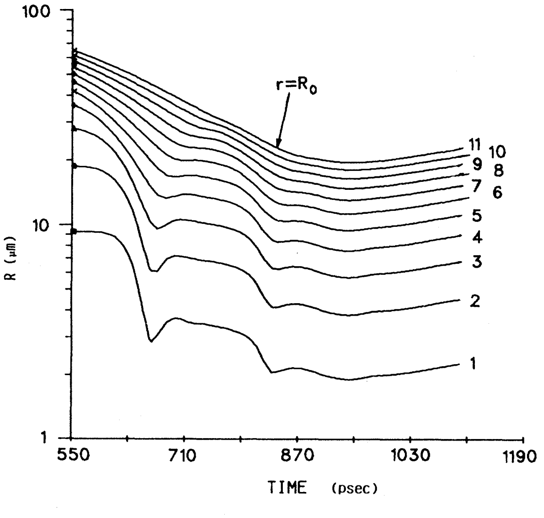

FIG. 6. Radii of various cells as a function of time for the same implosion as Fig. 4.

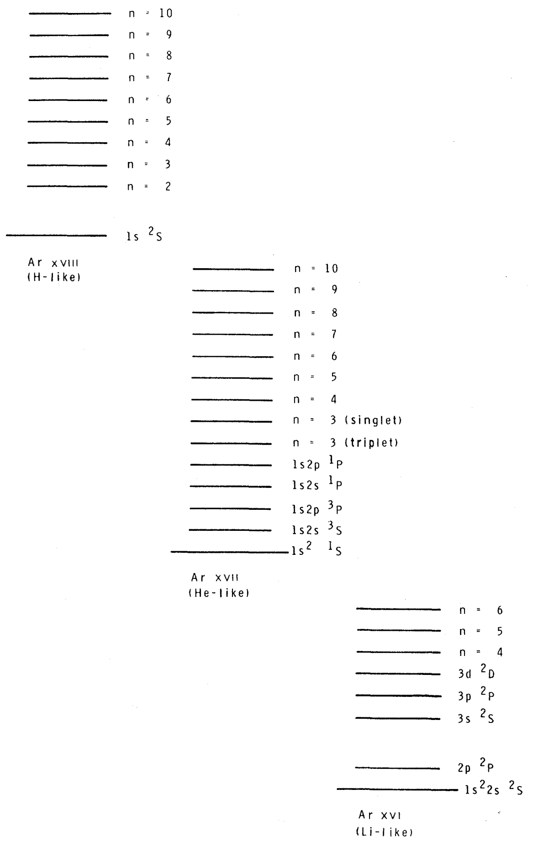

FIG. 7. Argon atomic level structure used in the collisional-radiative model.

In detail, the atomic model to which the K-shell radiation calculation was coupled consisted of a reasonably complete theoretical description of the argon K-shell structure inclusive of its major collisional and radiative couplings. Figure 7 displays the level structure employed, which contains excited states in hydrogen and heliumlike Ar XVIII and Ar XVII up to principal quantum number $n = 10$. In an analysis of the nonequilibrium behavior of moderate density hydrogen,[19] this value was found to be a convenient excited state cutoff which produces an adequately converged representation of the effective ionization and recombination rate coefficients between ground states that include cascade contributions from excited states.

The CR model also contains 47 line and 10 free-bound radiative couplings from the most significant K-shell emission processes. These couplings include both Balmer and Lyman series in Ar XVIII, Balmer and Lyman-type series in Ar XVII (including separate contributions from triplet and singlet Balmer-type lines up to $n = 7$), 1s2p-2p^2 and 1s2s-2s2p satellite lines in Ar XVII,[20] 2p-3d, 2s-3p, 2p-4d, 2s-4p, 2p-5d, and 2s-5p transitions in Ar XVI, and the free-bound couplings Z(bare nuclei)$\rightarrow$H($n=1$), $Z\rightarrow$H($n=2$), $Z\rightarrow$H($n=3$), H$\rightarrow$He($n=1$), H$\rightarrow$He($1s2p\ ^3P$), H$\rightarrow$He($1s2p\ ^1P$), H$\rightarrow$He($n=3$ triplet), H$\rightarrow$He($n=3$ singlet), He$\rightarrow$Li, and Li$\rightarrow$Be. (Z, H, He, Li, and Be denote Ar XIX, Ar XVIII, Ar XVII, Ar XVI, and Ar XV ionization stages, respectively). The energies of the ground and excited states (and hence of the lines and free-bound edges) were obtained from the tables of Bashkin and Stoner[21] or Kelly and Palumbo,[22] as well as from scaling laws for those high-lying states for which no tabulated data exists. The Einstein A coefficients of both Lyman and Balmer series have values that were extracted or extrapolated from a number of sources.[23–27] They were verified to yield well-behaved Fano plots of oscillator strength that merged smoothly into the continuum.

For Ar XVII the calculations of Lin and Johnson[28] were used to obtain the Ar XVII continuum oscillator strength. Because oscillator sum rules are satisfied and the radiative line couplings extend to $n=10$, the continuum edge behavior in this model can be studied as a dynamic process that is inseparable from line merging phenomena (and broadening). Thus, it will supplement other high-density approaches that modify both the level structure ("pressure ionization" of excited states) and the distributions of oscillator strengths[29]; i.e., pressure ionization *per se* has not been systematically included in the rate equations, nor have screening effects (on the collisional rate coefficients), although they tend to be small at the temperatures and densities encountered in these experiments.

The methods for calculating the collisional rate coefficients that are used in this model were carefully selected from the many techniques available in the literature.[30] The coupling to excited states occurs within the same ionization stage of the states; that is, they are coupled among themselves and to the ground states that are immediately adjacent, above and below. The ground and excited states of ionization stage Z are coupled to the ground state of ionization stage $Z+1$ by collisional ionization and photoionization. Electron-impact ionizations are calculated by the exchange classical impact-parameter method,[31] whereas photoionization cross sections were taken to be hydrogenic as computed by Menzel and Pekeris[32] or, in the case of the Ar XVII ground state, that calculated by Lin and Johnson.[28] The corresponding recombination rates were obtained by detailed balancing the ionization rates. Electron-impact excitations between ground and excited states and among excited states of an ion were calculated by the method of distorted waves[33,34] for levels with principal quantum number $n<6$ and by the semiclassical impact-parameter method[35] for $n>6$. Collisional deexcitation was again calculated by detailed balancing of these excitation rates. Photoionization and stimulated emission couplings for all bound-bound and free-bound allowed transitions were evaluated using a detailed solution of the radiative transport equation in spherical geometry[17,18]:

$$\left[\mu\frac{\partial}{\partial r}+\frac{1-\mu}{r^2}\frac{\partial}{\partial\mu}\right]I_\nu(r,\mu,t)=k_\nu(r,t)[S_\nu(r,t)-I_\nu(r,\mu,t)] \tag{3}$$

which was evaluated at $r=R(i,t)$ for $i=1,\ldots,11$. k_ν and S_ν are the absorption coefficient and source function, respectively (computed as the sums over overlapping line and continuum processes), and μ is the cosine of the angle between the radius and the x-ray direction. Coupling to the rate equations is achieved through the radiation energy density U_ν, defined by

$$U_\nu(r,t)=\frac{2\pi}{c}\int_{-1}^{1}d\mu\, I_\nu(r,\mu,t)\ , \tag{4}$$

while the emission power spectrum $P_\nu(t)$ is calculated from

$$P_\nu(t)=8\pi^2R_0^2(t)\int_{-1}^{1}d\mu\,\mu I_\nu(r=R_0,\mu,t)\ , \tag{5}$$

where R_0 is the radius of the Ar-DT region. Finally, we note that the smallness of the argon region ($<60\ \mu$m) and the relatively small change of the plasma temperature and density with time ($\sim$ps time scales) provides a justification for omitting the retardation term $(1/c)\partial_t I_\nu$ from Eq. (3). The effect of the time derivative terms in the rate equations, on the other hand, will be investigated in this paper.

The rate equations for the ion population densities, $[N_a(r,t)]$, are conveniently written in terms of the fractional ion densities, $f_a=N_a/N_{\rm Ar}$, where $N_{\rm Ar}=\sum_a N_a$:

$$D_tN_{\rm Ar}=-(\vec{\nabla}\cdot\vec{v})N_{\rm Ar}\ , \tag{6}$$

$$D_tf_a=\sum_b W_{ab}(N_e,T_e,U_\nu)f_b\ , \tag{7}$$

where the electron density

$$N_e=\sum_a Z_aN_a \tag{8}$$

must be determined self-consistently from the ion densities and

$$D_t=\frac{\partial}{\partial t}+(\vec{v}\cdot\vec{\nabla})\ , \tag{9}$$

is the time derivative within a fluid cell, i.e., attached to the Lagrangian coordinates of the fluid motion $v(r,t)$. In this paper, we will discuss both quasistationary[36,37] and collisional-radiative equilibrium (CRE) solutions to Eqs. (3)–(9). The solution to Eq. (6), along with the values of $T_e(r,t)$, is taken from the LASNEX calculation. For CRE to be valid $D_tf_a\equiv0$ for all states a: Solutions for the population densities are then found from

$$\sum_b W_{ab}(N_e,T_e,U_\nu)f_b=0\ , \tag{10}$$

where

$$N_e=\left[\sum_a Z_af_a\right]N_{\rm Ar} \tag{11}$$

was self-consistently determined from the f_a—not from the LASNEX calculation. In the case of the quasistationary approximation one assumes that only the excited states ($f_{a'}$) satisfy $D_tf_{a'}\simeq0$.

The equations $D_tf_{a'}=0$, for the collection of excited states (a') that lie within the ionization stage of ionic charge $+Z$, have the form

$$-\sum_{b'} W^Z_{a'b'}(N_e,T_e,U_\nu)f_{b'} = W^Z_{a'}f_Z + N_e\alpha^{Z+1}_{a'}f_{Z+1} , \tag{12}$$

where f_Z and f_{Z+1} are the relative ground-state population densities lying, respectively, below and above the excited-state manifold, and $W^Z_{a'b'}$ is the total rate (collisional plus radiative) for the excited-state—to—excited-state transition $b' \rightarrow a'$ ($b' \neq a'$), $W^Z_{a'a'}$ is the total decay rate of the excited state a', including deexcitation to the ground state below and ionization to the ground state above,

$$W^Z_{a'} = N_e X^Z_{a'}(T_e) + \int d\nu\, B^Z_{a'}(\nu)U_\nu$$

is the sum of electron and photon ground-state excitation rates, respectively, to the excited state a', and $N_e\alpha^{Z+1}_{a'}$ is the total rate (collisional and radiative) for direct recombination to excited state a'. The solution to Eqs. (12) is obtained in terms of the inverse matrix $(W^Z_{a'b'})^{-1}$ and can be used to define population coefficients $r^Z_0(a')$ and $r^Z_1(a')$ for each ionization state Z. They are defined by placing the solution to Eqs. (12) in the form[37]

$$f_{a'} = \mathscr{L}'(a')N_e r^Z_0(a')f_{Z+1} + \frac{g(a')}{g_Z}\exp[-\Delta E(a')/kT_e]r^Z_1(a')f_Z , \tag{12'}$$

where

$$\mathscr{L}'(a') = \frac{g(a')}{2g_{Z+1}}\left[\frac{h^2}{2\pi mkT_e}\right]^{3/2}\exp[\chi(a')/kT_e] \tag{13}$$

and $g(a')$, g_Z, g_{Z+1} are degeneracy factors for the excited states a' and the ground states of the Z and $Z+1$ ionization stages, respectively;

$$\Delta E(a') = E(a') - E_Z$$

and

$$\chi(a') = E_{Z+1} - E(a')$$

are likewise excitation and ionization energies of state a' from and to the Z and $Z+1$ ground states. Note that in LTE, $r^Z_0 + r^Z_1 = 1$. On substituting Eq. (12′) into the rate equations for the ground-state population densities f_Z one finds that

$$D_t f_Z = N_e\alpha^{Z+1}f_{Z+1} + N_e S^{Z-1}f_{Z-1} - N_e(S^Z + \alpha^Z)f_Z , \tag{14}$$

where S^Z and α^Z are effective ionization and recombination coefficients, respectively, that include, in addition to the direct ground-state—to—ground-state ionization and recombination rates, the contributions to these processes that proceed by cascade channels through the manifold of excited states.

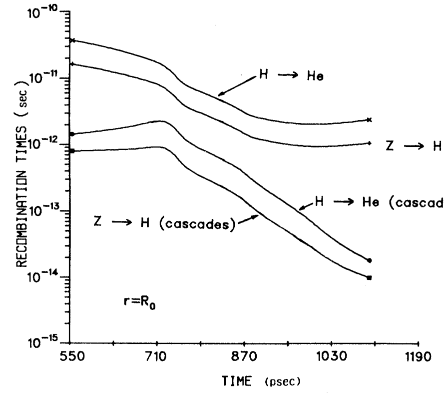

FIG. 8. Various recombination times calculated for the outermost cell.

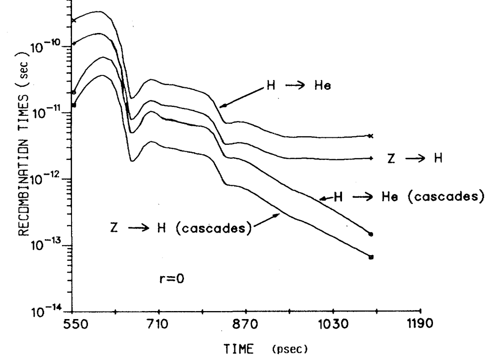

FIG. 9. Various recombination times calculated for the innermost cell.

To gain a better understanding of the way the above rate equation model functions as it processes the data in Figs. 4—6, we will discuss some of the behavior of $[N_e S^Z(r,t)]^{-1}$, $[N_e\alpha^Z(r,t)]^{-1}$, and $[\vec{\nabla}\cdot\vec{v}(r,t)]^{-1}$, the time constants that enter into the quasistationary theory.

Figures 8 and 9 provide comparisons between the calculated effective recombination times connecting bare nuclei (Z), hydrogenlike (H), and heliumlike (He) ionization stages (of argon), respectively, in the outer and innermost cells [$r = R(i=11,t)$ and $R(1,t)$] as well as between $Z \rightarrow$H and H$\rightarrow$He recombination times that are computed from the ground-state—to—ground-state rates. Figures 10 and 11 contain a set of corresponding comparisons between ionization times in the outer and inner cells. (The times for Li$\rightarrow$He ionization are less than 1 ps.) We will see later that peak emission occurs at ~860 ps, just before

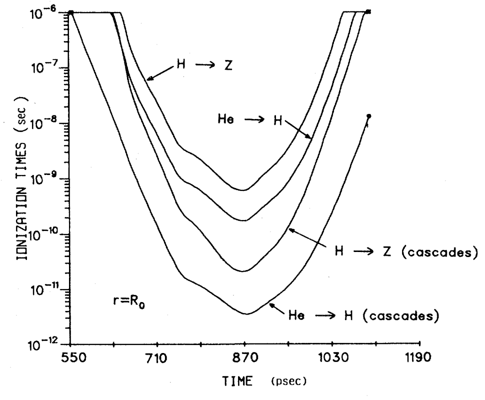

FIG. 10. Various ionization times for the outermost zone.

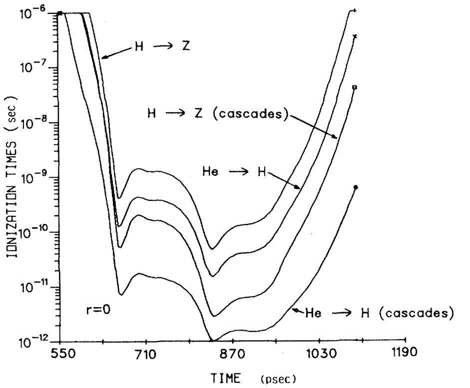

FIG. 11. Various ionization times for the innermost zone.

the minimum in ionization times. At this time the recombination rates are over an order-of-magnitude larger than the ionization rates in the outer cell, indicative of the fact that heliumlike argon remains the dominant ionization stage near the relatively cool glass boundary. Figures 8—11 also indicate that cascade through the excited states are the increasingly dominant pathway by which ground-state ionizations and recombinations occur at these high electron densities.

In a compressing or expanding plasma, one cannot ignore, necessarily, the effect of the velocity divergence on the rate equations. The compressibility time constant $1/|\vec{\nabla}\cdot\vec{v}|$ is computed at $r=R(1,t)$ and $r=R(11,t)$ as shown in Fig. 12. Spikes in these curves occur at times when the sign of $\vec{\nabla}\cdot\vec{v}$ is changing, that is, when compressions turn to expansions or rarefactions and vice versa (see Fig. 5). Just before peak emission (at 822 ps) a density change with a 20-ps time constant is induced in the center cell where the largest emission rates and ionization levels occur. In general, however, these time constants range widely around the $\frac{1}{10}$th nanosecond level and can be, at times, competitive with the ionization times shown in Figs. 10 and 11, although they are not at the time of interest: peak emission.

The radiation picture that emerges from the implosion and ionization dynamics, as shown in Figs. 4—12 is complicated by several factors. The Ar-DT fuel mixture was selected to minimize effects of opacity on the ionization level and emission spectrum; nevertheless, under compression, both hydrogen and heliumlike resonance lines become optically thick. At peak emission, the $1s^2$-$1s\,2p$ line has an opacity of 71 while the $1s$-$2p$ line's opacity is 3.6 at line center. As was shown in the last paper of Ref. 5, the optical pumping effect (especially in the center cell) of these lines is large. The temperature and density gradients also play important, sometimes opposing, roles in determining levels of ionization and emission. For example, at peak emission, the center cell is the hottest and least dense of all the cells. Higher density tends to suppress ionization while the higher temperature promotes it. In these cases, which are also often encountered in discharge tubes, the emission spectrum is formed at the center and shaped by opacity near the surface. This ionization behavior is confirmed in Figs. 13 and 14, which show the K-shell ground-state population densities at $r=0$ and $r=R(11,t)$

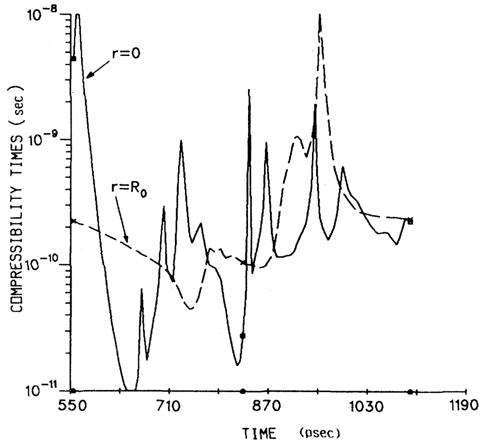

FIG. 12. Compressibility time ($1/|\vec{\nabla}\cdot\vec{v}|$) for the inner and outermost zones.

for both collisional-radiative equilibrium (CRE) (solid line) and quasistationary (dashed line) solutions to Eqs. (2) to (9).

As expected, rapid changes in ionization, on 10-ps time scales, cause the quasistationary solution for the ground states to lag behind the CRE solution. As indicated by the line drawn at 640 ps (in Fig. 13), differences in these solutions can be large. Nevertheless, due to the compression, which sharply diminishes the ionization and recombination times, this comparison demonstrates that the CRE assumption is generally very good in the core region of this Ar-DT implosion. The difference in the computed time-integrated, quasistationary and CRE emission spectra was less than 1% in absolute magnitude (even though a final state of shock heating occurs around the time of peak emission). Qualitatively they were identical.

A final question of interest concerning population densities is the degree to which argon excited states come into local thermodynamic equilibrium (LTE) with the ground states during the implosion. The behavior of the popula-

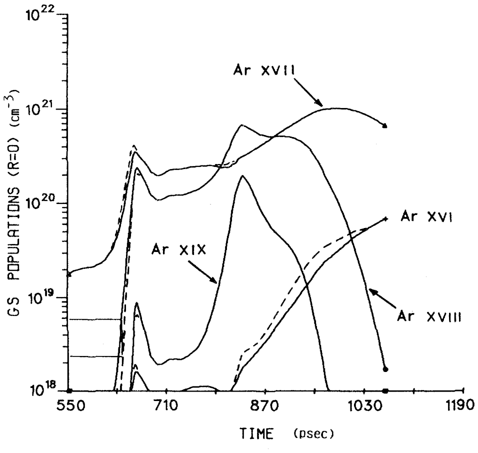

FIG. 13. Ground-state (GS) population densities for Ar XVI through Ar XIX for both CRE (solid line) and quasistationary (dashed line) solutions at $R=0$.

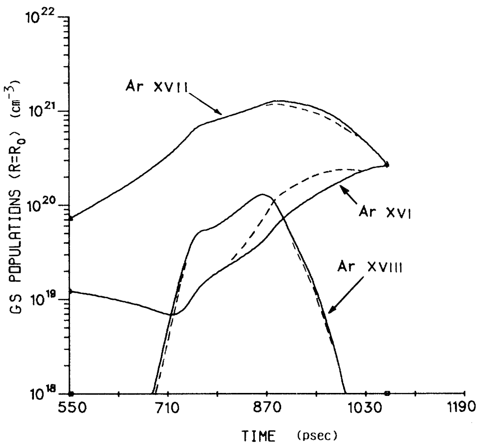

FIG. 14. Ground-state population densities for Ar XVI through Ar XVIII for both CRE (solid line) and quasistationary (dashed line) solutions at $r = R_0$.

tion coefficients provides the answer. Calculations of these coefficients confirm that states with principal quantum numbers greater than 3 remain in LTE with the Ar XVIII ground state throughout the implosion. The overall ionization distribution is not, however, in LTE. The Ar XVIII excited states behave similarly to the Ar XVII states; in particular, the $n = 3$ state comes within 90% of LTE with Ar XIX at peak emission as the simple theoretical estimate given in the introduction suggested.

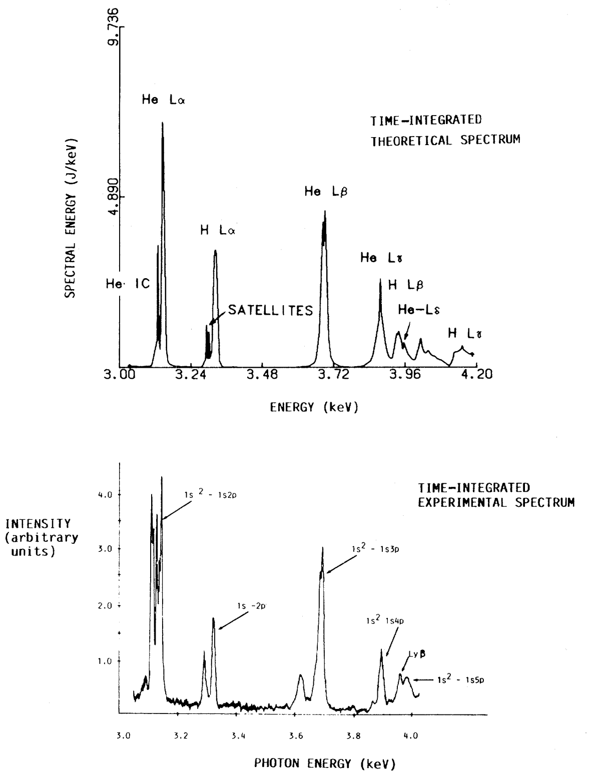

FIG. 15. Comparison of time-integrated experimental spectrum and its corresponding theoretical calculation.

Line profile calculations are also a critical component of this spectral modeling. The spectral profiles that were used in the radiative transfer and rate equation calculations were computed based on a theory[9,14] which treats the electron collisions by an impact approximation. This allows for the level splittings induced by (1) the ion electric fields, (2) the finite duration of the collisions, and (3) the screening of the electric fields. The effects of inelastic collisions are also included by parametrically modeling calculations carried out in the distorted-wave approximation.

Ion effects were calculated in the approximation of the quasistatic Stark effect. The electric microfield distribution functions used were those calculated by Hooper.[38] In this case the microfields were those appropriate for the DT mixture.

The asymmetry of the two electron line profiles is the result of the loss of degeneracy of the Hamiltonian with respect to angular momentum quantum numbers. The energy levels of the S, P, D, etc., states within a multiplet, and the mixing coefficients of the singlet and triplet multiplets, were obtained from the work of R. Cowan.[39] Doppler broadening, as well as an approximate correction for ion dynamic effects and fine-structure splitting, were added by performing a convolution of the Stark profile with a Gaussian of width

$$\Delta = (\Delta_{\mathrm{Dop}}^2 + \Delta_C^2 + \Delta_{\mathrm{fs}}^2)^{1/2} ,$$

where Δ_{Dop} is the Doppler halfwidth, Δ_C is the ion dynamic correction, and Δ_{fs} is the fine-structure splitting. The latter two quantities are approximate; moreover, this procedure is valid only if their contribution to the broadening is small.

Coupling of populations to the radiation field in the rate equations depends critically on the shape of optically thick lines (in the present case, principally $1s$-$2p$ and $1s^2$-$1s\,2p$) as functions of density and temperature. In the present imploded argon spectra, photon coupling to $n > 3$ states is not a strong effect; however, the line shapes and widths of the helium Lyman-type β, γ, and δ, and the hydrogen Lyman β lines are important diagnostically.

IV. COMPARISON OF THEORY AND EXPERIMENT

In this section we describe a comparison between theoretical calculations and experiment for a typical laser shot to illustrate the capabilities of the modeling.[40] In Fig. 15 we show a typical, time-integrated spectrum (similar to those in Fig. 2) and its corresponding theoretical simulation (including source broadening). This is the same shot whose behavior was modeled in Figs. 4—6. There is a good overall agreement between the experiment and the calculation. The target that produced this imploded spectrum had a 240-μm-diameter glass shell coated with 35 μm of plastic (CH$_2$). The complex of satellites on the low-energy side of the $1s^2$-$1s\,2p$ and $1s^2$-$1s\,3p$ lines are not modeled in the present calculation.

In Fig. 16, we show an expanded trace of the $1s^2$-$1s\,3p$ line calculation and corresponding experimental points. The method for calculating the deviation between theory and experiment (described in Sec. II) is applied here to the comparison between the CRE theory and the experimental spectrum. The fit factor is about 2 times the ideal fit (described in the experimental section). This gives a confi-

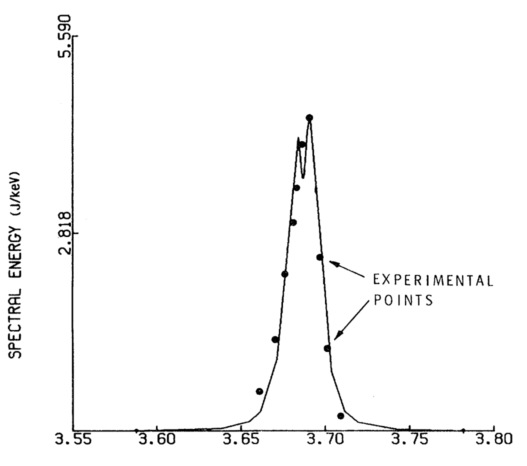

FIG. 16. Comparison of time-integrated experimental profile of the $1s^2$-$1s\,3p$ line and its corresponding theoretical calculation.

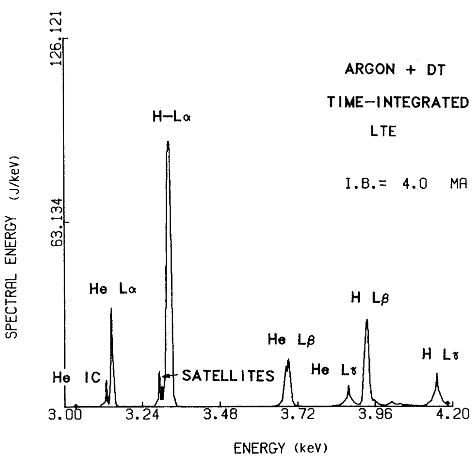

FIG. 17. Calculation of the same spectrum as in Fig. 15 under the assumption of LTE conditions.

dence level of about ±50% in the estimate of average density during the compression. This confirmed an average compressed electron density of about 3×10^{23} cm^{-3} for this particular shot. The more complete CRE model gives (in this case) a slightly higher value for compressed density than the simple model (Sec. II). This is because the peak emission occurs at a significantly different time than peak compression. The CRE model accounts for the variations in density throughout compression (in predicting the time-integrated spectrum) where the simple model does not. A similar fit factor was obtained in the profile analysis of the $1s^2$-$1s\,4p$ line.

The hydrodynamic calculation is constrained by laser input parameters and several experimentally measured quantities. The laser energy input (used in the simulation) follows the measured laser temporal profile. The absorbed energy fraction was consistent with ion calorimetry measurements.

The hot-electron spectrum used in the hydrodynamic calculation was taken to be consistent with measurements of hard x-ray bremsstrahlung measurements (in this case about 200 keV). The results of these calculations are somewhat sensitive to the choice of T_{hot}. Uncertainties in the hot temperature may account for some of the deviation between theory and experiment.

In addition to line spectra the adequacy of the hydrodynamic simulations were checked against other measured quantities. The measured neutron yield from DT fusion agreed with calculations to within a factor of 2—3 (neutron yield depends on compressed core temperatures to the sixth power). The ion temperature was measured by the spread in the measured fusion neutron spectrum. This, in general, agreed with the calculated value to within about ±30%. There was no direct atomic spectral signature of ion temperature since Doppler broadening was too small to be measured. Uncertainties in the hot temperature may account for some of the deviation in the relative strengths of hydrogenlike and heliumlike lines in the theoretical and experimental spectra.

The delay between the onset of laser irradiation and the peak of neutron production was measured by time resolved neutron detectors. In the present case this was about 1 ns, which was in good agreement with the calculated value.

In all, the agreement between theory and experiment in Fig. 15 is quite good; the major discrepancy, which occurs in the relative heights of the hydrogenlike and heliumlike lines, can be attributed to the sensitivity of these line ratios to the temperature peaks in the different cells of the argon core. There are a number of possible reasons for the slightly greater relative strength of the calculated hydrogenlike to heliumlike lines, including, one might think, the possibility that greater spatial resolution than eleven cells is needed in defining the temperature gradients in the argon region. There is some evidence to indicate,[41] however, that calculations based on twice the number of zones reflect some changes but not of a nature as to significantly alter our results or conclusions. Mainly, it should be pointed out that, to get as good an agreement, as is seen in Fig. 15, it is essential that one not make the assumption that the argon populations are in, or close to, LTE. In Fig. 17 we show the emission spectrum that was calculated when LTE population densities were used in the postanalysis of Figs. 4—6. The spectrum was computed using the same eight Stark profiles and folding in 4 mÅ of source broadening as was done in the CRE calculation. The hydrogenlike Lyman-series lines not only completely dominate the corresponding heliumlike lines in this case, but the absolute strength of all the lines is significantly greater than in the CRE spectrum of Fig. 15. In addition to the time-integrated calculation shown in Fig. 15, other outputs from the CR model are shown in Figs. 18—21, which illustrate other aspects of the dynamics of radiative emission from these high-density implosions.

Figure 18 shows the calculated power output above a kilovolt, partitioned into three spectral intervals 1.0—3.0, 3.0—4.1, and 4.1—13.5 keV. The upper limit of 13.5 keV is the cutoff for the calculated spectrum. The powers in each interval peak at a different time and, overall, more energy is radiated into the (1.0—3.0)-keV continuum than is emitted into the (3.0—4.1)-keV line and continuum interval (~0.2-J radiated). The (3.0—4.1)-keV emissions

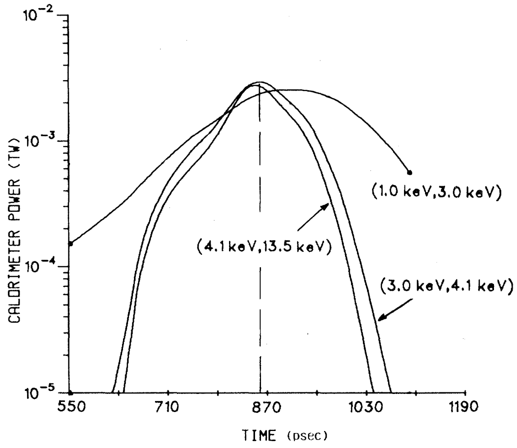

FIG. 18. Calculated power outputs above 1 keV.

peak at ~862 ps with a separation between the $\frac{1}{2}$-power points of approximately 105 ps. In this time interval, significant temperature and density changes occur in the Ar-DT core. Note that peak emission occurs between the times for peak temperature (830 ps) and peak density (950 ps). In Figs. 19 and 20, for comparison with the time-integrated spectrum, we show power spectra at times of peak emission and peak compression. It is important to note the differences between the two and the experiment. At peak emission, the hydrogenlike lines are relatively strong while at peak compression they are weaker than the experimental spectrum.

The 105-ps interval for strong line emission precedes the moment when the Ar-DT region has collapsed to its smallest radius. Thus, a somewhat higher compression is attained than is measured by the x-ray spectrum in this case.

V. SUMMARY AND CONCLUSIONS

The matching of time-integrated experimental x-ray spectra with theoretical spectra (over broad energy ranges) in well characterized implosion experiments, of the type described in this paper, can provide valuable confirmations of our understanding of laser-driven implosion dynamics. It can also provide important tests of theoretical atomic physics computational procedures and models.

Reasonably good agreement has been obtained between the theoretical modeling and time-integrated spectra. This gives confidence that the basic method for modeling this complicated phenomenon is essentially correct.

The spectra in Figs. 19—20 demonstrate an interesting point about average temperature measurements in a transient, moving plasma where two sets of lines may be formed at different times, at different places, and under different plasma conditions. Continuum shapes, for example, of the free-bound continuum $(Z \rightarrow \mathrm{H})$ are, in general, preferred over line ratios as an average temperature indicator. The curves in Fig. 21 show the result of computing temperatures from what would be measured by two calorimeter readings at 4.43 and 9.3 keV (carried out in the calculation). One was time resolved and one time integrated. The peak in the time resolving calculation almost coincides with the peak in (4.1—13.5)-keV emission and has a value of 930 eV; the time-integrating calculation, on the other hand, yields a final temperature of only

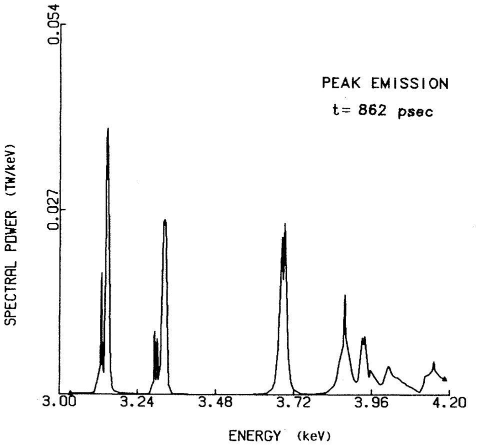

FIG. 19. Power spectrum at 862 ps into the implosion.

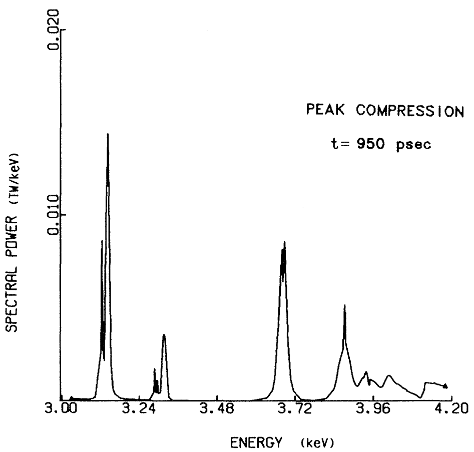

FIG. 20. Power spectrum at 950 ps into the implosion.

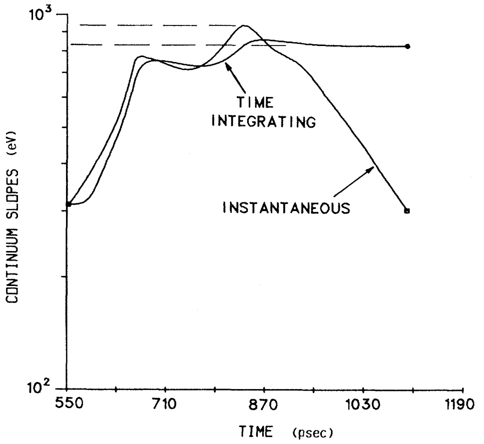

FIG. 21. Calculated temperature determinations.

820 eV (see Fig. 4). One virtue of obtaining average temperatures from continuum slopes is that the average is relatively well defined (though it will underestimate the peak temperature).

From a theoretical point of view, coupling of the rate and radiative transfer equations to the hydrodynamic input data achieves four goals. One, the effect of optical pumping is correctly included in the determination of the argon excited states. Two, the calculated line emission spectrum automatically contains the necessary opacity corrections to the underlying Stark profiles. Three, the computed spectrum contains the effects of the core region temperature and density gradients. And four, the instantaneously calculated argon power spectra can be time integrated for comparison with the experimental spectrum. A fifth advantage to the calculation, not tested in this experiment, is that it looks at the full range of radiated *K*-shell energies, not just in the (3.0—4.1)-keV range.

Several interesting extensions of this work suggest themselves. First, because of the low concentration of argon, the (collisionally dominated) CRE approximation was quite valid, i.e., optical pumping and transient emission effects were minimized. Moreover, the argon concentration was low enough and the compression weak enough that opacity and many-body corrections to the emission spectrum were also minimized. It would be useful to extend this analysis to pure argon fill at higher density, such as has been observed experimentally.[1]

It would be useful to extend this experimental-theoretical analysis either to pure argon fills or to the analysis of experimental spectra at higher-compression densities $>10^{24}$ e/cm^3, where one expects to make the transition into a physics regime where many-body effects begin to be important.[42] In some pure argon compressions, for example, one expects the argon region to contain large temperature and density gradients at times before peak compression is reached (larger than in Figs. 4 and 5). Issues relating to the degree of spatial resolution that is needed in modeling implosion and x-ray emission histories can be fruitfully investigated in these cases. Nevertheless, since analyses of laser-produced experimental spectra have been heretofore essentially "one-cell" analyses, the calculations described in this paper already constitute a major step forward in the spatial resolution of plasma conditions.

The timing of the implosion was such that there was no contribution to excitation from direct suprathermal electron pumping. It would be interesting to extend the present detailed spectrum analysis to cases where effects from suprathermal pumping might be observed.

VI. COMMENTS ON NUMERICAL ISSUES

In a recent article, R. W. Lee[43] presented a set of arguments regarding the convergence of solutions to coupled rate and radiative transfer equations. He argued from an analogy between time-dependent radiative transfer (TDRT) calculations and the "Λ-iteration" method of time-independent calculations. (One method is a forward going time step procedure while the latter method effectively time steps in place—often starting from initial conditions that are far removed from the final equilibrium solution.) Because the Λ-iteration method can require a great many iterations to converge in cases of high opacity—especially when such methods of solution are initiated far from equilibrium—Lee concluded that the TDRT method will converge only very slowly in these cases and, therefore, that it is "doubtful that TDRT calculations will produce the correct spectral output in general because the coupling of the radiation field to the rate equations which can, and usually does, have both local and global effects for different frequencies, is not treated consistently."

We would like to make a few comments of clarification about this statement since there are three distinct issues that are raised by it: (1) coupling consistency, (2) the convergence of solutions and their time step requirements, and (3) the correctness of computed spectral outputs. From the experience gained from the calculations that were reported on in this paper we conclude that (1) coupling consistency between rate and radiative transport equations can (and must) be achieved, (2) convergence is stable but indeed a function of the rate of change of plasma conditions and therefore of the number of time steps taken, and (3) it does not appear to be doubtful that correct spectral outputs can, in general, be obtained—all the more so if they are only required to the degree of absolute accuracy with which they are obtained experimentally. While the spatial resolution behavior of our post-analysis calculations was not investigated, the temporal convergence behavior was, first by time stepping with the hydrodynamics calculation and then by doubling and quadrupling the number of steps. Moreover, the convergence of the time-dependent CRE calculation was also verified by Λ iterating for a well converged solution at an instant in time late in the implosion. The time-integrating and the instantaneous rate radiative transfer equation solutions were found to agree to better than 1% at this randomly selected time.

In summary, the radiation field, rate equation couplings can be made to be self-consistent and, hence, should not be the issue. The time it takes to arrive at a steady state depends on the degree of departure of the system from equilibrium and, also on the slowest of the rate equation time constants. The time step selection may be governed by the fastest rate process in the rate equations; hence, the number of time steps needed to numerically integrate into equilibrium in both high, and low-density regions may be large for an improperly posed problem due to the global nature of radiation field couplings. However, there is no need to doubt that an accurate spectrum calculation can be carried out in this fashion.

ACKNOWLEDGMENTS

The authors would like to acknowledge many useful discussions with Professor Hans Griem. Eldon Linnebur provided invaluable assistance with the hydrodynamic modeling. Early work on LASNEX modeling by Roger Kopp provided some valuable starting points. The neutron measurements described here were performed by Tai Ho Tan and Art Williams. We would like to acknowledge the essential work of the Los Alamos target fabrication and Helios laser operations teams in performing these experiments. This work was supported jointly by the U. S. Department of Energy and the Defense Nuclear Agency.

[1] B. Yaakobi, S. Skupsky, R. L. McCrory, C. F. Hooper, Jr., H. Deckman, P. Bourke, and J. M. Soures, Phys. Rev. Lett. 44, 1072 (1980); B. Yaakobi *et al.*, Opt. Commun. 43, 343 (1982).

[2] A. Hauer *et al.*, Phys. Rev. Lett. 45, 1495 (1980).

[3] J. M. Auerbach *et al.*, Phys. Rev. Lett. 44, 1672 (1980).

[4] B. Yaakobi *et al.*, Phys. Rev. Lett. 39, 1526 (1977); B. Yaakobi *et al.*, Phys. Rev. A 19, 1247 (1979); K. Mitchell, D. van Hulsteyn, G. McCall, P. Lee, and H. Griem, Phys. Rev. Lett. 42, 232 (1979).

[5] J. P. Apruzese, P. C. Kepple, K. G. Whitney, J. Davis, and D. Duston, Phys. Rev. A 24, 1001 (1981); K. G. Whitney, J. Davis, and J. P. Apruzese, *ibid.* 22, 2196 (1980); K. G. Whitney and P. C. Kepple, J. Quant. Spectrosc. Radiat. Transfer 27, 281 (1982).

[6] H. R. Griem, *Plasma Spectroscopy* (McGraw-Hill, New York, 1964) (available from University Microfilms).

[7] Source size determinations from slitted spectrograph images assumed spherical symmetry. See, for example, M. M. Mueller, Opt. Lett. 4, 351 (1979).

[8] A. J. Burek, Space Sci. Inst. 2, 53 (1976).

[9] H. R. Griem, M. Blaha, and P. C. Kepple, Phys. Rev. A 19, 242 (1979).

[10] C. F. Hooper, Jr. and L. A. Woltz, University of Florida Technical Report No. DE-ASOS-76DP400016 (unpublished).

[11] A. Hauer, in *Spectral Line Profiles* (de Gruyter, Berlin, 1981), p. 295. In addition to the temperature dependence of line profiles this reference also discusses other aspects of theoretical line profile calculations relevant to plasma density diagnostics.

[12] R. Benjamin, P. B. Lyons, and R. H. Day, Appl. Opt. 16, 393 (1976). Calibration procedures such as those described in this reference are performed periodically.

[13] H. R. Griem, *Spectral Line Broadening by Plasmas* (Academic, New York, 1974).

[14] H. R. Griem and P. C. Kepple, *Spectral Line Profiles* (de Gruyter, Berlin, 1981), p. 391.

[15] G. Zimmerman and W. Kruer, Comments Plasma Phys. Controlled Fusion 2, 85 (1975).

[16] W. A. Lokke and W. H. Grasberger, Lawrence Livermore Laboratory, Report No. UCRL 52276 (unpublished).

[17] P. C. Kepple and K. G. Whitney, U. S. Naval Research Laboratory Report No. 4565 (unpublished) performed under contract to Los Alamos National Laboratory.

[18] K. G. Whitney, J. Davis, and J. P. Apruzese, in *Cooperative Effects in Matter and Radiation,* edited by C. M. Bowden, D. W. Howgate, and H. R. Robl (Plenum, New York, 1977), p. 115.

[19] M. Cacciatore and M. Capitelli, Z. Naturforsch. 29a, 1507 (1974).

[20] D. Duston and J. Davis, Phys. Rev. A 21, 932 (1980).

[21] S. Bashkin and J. O. Stoner, Jr., *Atomic Energy Levels and Grotrian Diagrams* (North-Holland, Amsterdam, 1978), Vol. II.

[22] R. L. Kelly and L. J. Palumbo, Naval Research Laboratory Report No. 7599 (unpublished).

[23] A. Lindgard and S. E. Nielsen, At. Data Nucl. Data Tables 19, 553 (1977).

[24] B. C. Fawcett, At. Data Nucl. Data Tables 22, 473 (1978).

[25] C. D. Lin, W. R. Johnson, and A. Dalgarno, Phys. Rev. A 15, 154 (1977).

[26] C. Laughlin, J. Phys. B 11, L391 (1978).

[27] W. Wiese, M. Smith, and B. Miles, *Atomic Transition Probabilities* (U. S. GPO, Washington, DC, (1969), Vol. II.

[28] C. D. Lin and W. R. Johnson, J. Phys. B 12, 1677 (1979).

[29] J. C. Weisheit and B. W. Shore, Astrophys. J. 194, 519 (1974).

[30] D. Duston and J. Davis, J. Quant. Spectrosc. Radiat. Transfer 27, 267 (1982); the table of rate coefficients that were used in these calculations was constructed by D. Duston.

[31] A. Burgess, H. P. Summers, D. M. Cochrane, and R. W. P. McWhirter, Mon. Not. R. Astron. Soc. 179, 275 (1977).

[32] D. H. Menzel and C. L. Perkeris, Mon. Not. R. Astron. Soc. 96, 77 (1935).

[33] J. Davis, P. C. Kepple, and M. Blaha, J. Quant. Spectrosc. Radiat. Transfer 16, 1043 (1976).

[34] A. L. Merts, J. B. Mann, W. D. Robb, and N. H. Magee, Jr., LASL Report No. 8267 (1980) (unpublished).

[35] E. Oran and J. Davis, J. Appl. Phys. 45, 2480 (1974).

[36] D. R. Bates, A. E. Kingston, and R. W. P. McWhirter, Proc. R. Soc. London 267, 297 (1962).

[37] T. Fujimoto, J. Phys. Soc. Jpn. 47, 265 (1979); 47, 273 (1979); 49, 1561 (1980); 49, 1569 (1980).

[38] C. F. Hooper, University of Florida Report No. 8820309 (U. S. Dept. of Energy contract) (unpublished); see also, J. T. O'Brien and C. F. Hooper, Phys. Rev. A 5, 867 (1972).

[39] See, for example, R. D. Cowan, J. Opt. Soc. Am. 58, 808 (1968).

[40] We have chosen first to model an intermediate density case (with $n_e \simeq 3\times 10^{23}$ cm^{-3}). This was chosen because we had the greatest confidence in modeling (rate coefficients, etc.). Currently, higher-density cases are being considered.

[41] D. Duston, R. W. Clark, J. Davis, and J. P. Apruzese, Phys. Rev. A 27, 1441 (1983).

[42] J. Davis and M. Blaha, J. Quant. Spectrosc. Radiat. Transfer 27, 307 (1982); R. More, *ibid.* 27, 345 (1982).

[43] R. W. Lee, J. Quant. Spectrosc. Radiat. Transfer 27, 243 (1982).